Numerical Simulations Based Evidence of Impingement Free Sound Production During Vortex-Nozzle Interaction in Solid Rocket Motors

Hirschberg, Lionel; Hulshoff, Steven; Schuller, T.; Schram, C; Collinet, J.

Numerical Simulations Based Evidence of Impingement Free Sound Production During Vortex-Nozzle Interaction in Solid Rocket Motors

L. Hirschberg[*]

ArianeGroup, CentraleSupélec, von Karman Institute for Fluid Dynamics.

S. J. Hulshoff[†]

Faculty of Aerospace Engineering, Delft University of Technology.

T. Schuller[‡]

Insitut de Méchnique des Fluides, IMFT, Univesité de Toulouse, France.

C. Schram [§]

von Karman Institute for Fluid Dynamics.

J. Collinet [¶]

ArianeGroup.

Dedicated numerical simulations of vortex-nozzle interaction indirect noise in solid rocket motors (SRMs) are presented. It is assumed that the flow in the nozzle and hence the sound radiation is not significantly influenced by the global acoustic oscillation of a SRM. Therefore, the study is limited to the acoustic response of a semi-infinite pipe terminated by a choked nozzle. The nozzle considered here is placed flush in a wall forming a right angle to the walls of the combustion chamber. The study focuses on where sound is produced due to vortex-nozzle interaction. The presented results indicate that sound is produced when the vortex is on its approach to the nozzle, rather than by impingement of the vortex on the nozzle walls.

I.   Introduction

Self-sustained high-amplitude acoustic oscillations can occur in solid rocket motors (SRMs). The oscillation frequency is close to the first longitudinal acoustic mode of the combustion chamber with frequencies $f \sim c/(2L)$, where L is the length of the combustion chamber and c is the speed of sound.[1–4, 13] In small SRMs direct combustion noise is often the driving source. In large SRMs, the oscillations occur due to the establishment of a feedback loop, in which vortices which are shed upstream of the nozzle produce indirect noise through vortex-nozzle interaction.[1, 4, 8, 11, 13, 14] The resulting acoustic pulses travel upstream, and reflect from the end of the combustion chamber producing the longitudinal acoustic standing wave. This wave in turn causes vortex shedding, leading to a self-sustained process.

To shed more light on this process, this paper will consider the sound production of vortex-nozzle interactions in isolation. In doing so, it is assumed that once the vortex is shed, the acoustic oscillation does not affect the sound production directly. This will be the case if the velocity fluctuations u' associated with the oscillation remain small compared to the main flow velocity U upstream from the nozzle, typically $u'/U < 10^{-1}$.

---

[*]PhD student, Laboratoire EM2C, CNRS, CentraleSupélec, Université Paris Saclay, 3 Rue Joliot Curie, 91190 Gif-sur-Yvette, France, AIAA Student Member.

[†]Associate Professor, Faculty of Aerospace Engineering, Delft University of Technology, Kluyverweg 1, 2629 HS Delft, the Netherlands

[‡]Professor, Institut de Méchnique des Fluides, IMFT, Univesité de Toulouse, CNRS, 2 allée du Professeur Camille Soula, 31400 Toulouse, France

[§]Professor, von Karman Institute for Fluid Dynamics, Waterloosesteenweg 72, 1640 Sint-Genesius-Rode, Belgium.

[¶]R & T Engineer, ArianeGroup, 51-61 route de Vernueil, 78133 Les Mureaux, France.

American Institute of Aeronautics and Astronautics

Therefore, instead of considering a closed combustion chamber, the vortex-nozzle interaction is studied in a semi-infinite channel terminated by a choked nozzle. In the present paper, this is done using dedicated numerical simulations. These were carried out using the Euler Internal Aeroacoustics (EIA) code.[12,17,19] This code has previously been used to study vortex-nozzle interaction both for subcritical and choked contractions.[12,19]

Considering just the vortex-nozzle nozzle interaction, instead of full scale high fidelity numerical simulations of a SRM, has a number advantages. Firstly, the relative low cost of the simulations ensures grid-independent results can be maintained while performing extensive parameter studies. Secondly, considering only part of the process in isolation simplifies the interpretation of the obtained results. These simulations have already yielded a scaling law for vortex-nozzle interaction induced sound,[12] and have been used to develop a lumped element model of the sound source.[11] The flow is assumed to be frictionless. To further reduce the numerical effort needed a two-dimensional planar flow is considered.

Although it is known that vortex-nozzle interactions produce sound, the mechanism is not well established. Indeed, a process described as "impingement" is put forward by Flandro.[7] It is, with a large degree of certainty, inspired by Rockwell's work on oscillations of imping shear layers.[20] From Flandro's[7] paper it is unclear what is exactly meant by impingement. However, the fact that Rockwell[20] is cited leaves the reader to infer that sound is produced due to a vortex physically striking an impingement surface, viz. the nozzle walls. This appears to be the interpretation of Fabigion et al.[4] and Culick[2] . It is certainly the interpretation of Dotson et al.[3] and Ferretti et al.[5,6] Impingement could also be interpreted as "physical" contact involving splitting of the vortex, and subsequent partial inhalation of the vortex due to local flow separation on the nozzle walls.

In this paper results of a numerical investigation of vortex-nozzle interaction are reported. The objective of the investigation is to establish if the sound produced by vortex-nozzle interaction can occur without impingement. The nozzle geometry used for the simulations is described in section II. Simulation results relating the position of the vortex during the sound production process and the shape of the upstream traveling acoustic pulse are shown in section III. In appendix A, a brief description of the Euler Internal Aeroacoustics code (EIA) and its use for vortex-nozzle interaction simulations is given. The generation of a mesh is described in appendix C. The establishment of a stationary base flow used to initialize the domain for vortex-nozzle interaction simulations is described in appendix D. The generation of a vortex and the boundary conditions used for vortex-nozzle interaction simulations are detailed in appendix E.

II. Nozzle geometry

For the present study, a nozzle with an inlet containing a right angle corner is considered, as illustrated in Fig. 1.

Figure 1. Nozzle inlet geometry considered: a nozzle inlet with a right angle corner.The flow direction is from left to right. The ratio of nozzle inlet to nozzle throat cross-sectional area A_1/A^* can be varied to set the upstream Mach number M at the inlet.

Sketches of a right angle inlet nozzle configuration for cylindrical and rectangular configurations are shown in Fig. 2 (a) and (b), respectively. Fig. 2 is used to illustrate the relation between a rectangular channel configuration (two-dimensional plane) used in the model and the actual cylindrical configuration of e.g. scale experiments. The relation between these two configurations is through an equal contraction ratio of the upstream and throat surfaces viz. $S_1/S_2 = (R_1/R_2)^2$. The upstream pipe radius R_1 and throat radius R_2 of the cylindrical tube relates to the upstream channel height S_1 and the throat channel height S_2 of

American Institute of Aeronautics and Astronautics

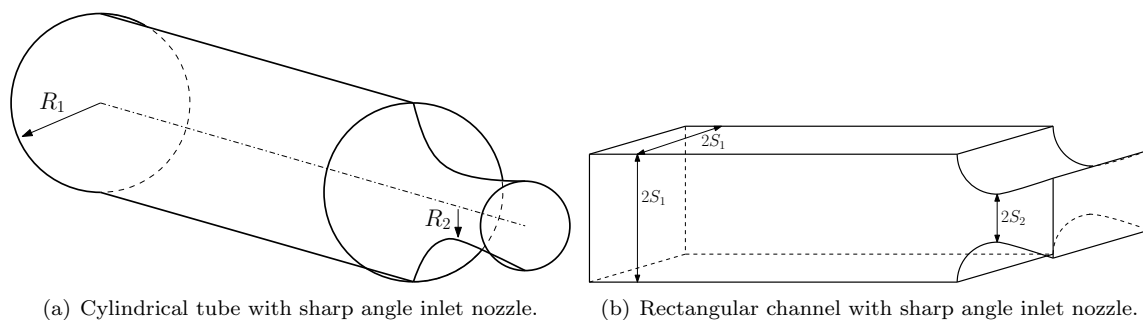(a) Cylindrical tube with sharp angle inlet nozzle.   (b) Rectangular channel with sharp angle inlet nozzle.

Figure 2. Relation cylindrical and rectangular configuration. Where the relation between the two configurations is trough the contraction ratio $S1/S2 = (R1/R2)^2$ with $R_1 = S_1\sqrt{4/\pi}$ and $R2 = \sqrt{2S_1S_2/\pi}$.

the rectangular channel as follows $R_1 = S_1\sqrt{4/\pi}$ and $R_2 = \sqrt{2S_1S_2/\pi}$. To a fair degree of approximation (one-dimensional model) the ratio S_1/S_2 determines the Mach number of the uniform flow approaching the choked nozzle.

The right angle inlet geometry shown in Fig. 1 was drawn using Henrici's[10] conformal mapping as used in previous analytical models.[13, 15] Although this does not precisely correspond to a geometry used in scale-model experiments, similar right angle inlet geometries have been used in both hot-gas (with combustion) and cold-gas scale model experiments.[1, 9]

III.   Vortex-Nozzle interaction

The vortex is generated by introduction of a momentum source term in the equations of motion. The details of the base flow and the vortex generation procedures are described in appendices D and E. Once the vortex generation process is completed, the vortex circulation, Γ, is conserved in the numerical domain. The mature vortex is convected downstream with the base flow, where eventually it passes through the nozzle (Fig. 3). One observes that during the ingestion process, no impingement of the vortex and the contraction wall takes place. This is consistent with the use of Euler equations for which vorticity is convected along streamlines. This can be expected to be a good approximation of the high-Reynolds-number flows encountered in this part of the SRM. Where the viscous boundary layers on the inlet wall of the nozzle are very thin and the flow acceleration reduces the likelihood of flow separation. As such, for typical vortex circulations $|\Gamma/(US_1)| < 1$ one does not expect any boundary layer separation induced by the vortex and subsequent annihilation of said vortex.

Results shown in Fig. 3 are for a vortex of dimensionless circulation $\tilde{\Gamma} \equiv \Gamma/(US_1) = -0.86$, where U is the upstream velocity. This value is in the expected range for SRMs.[12] The vortex core-radius is $R_\Gamma = 0.3S_1$. The upstream Mach number used in the simulations is fixed to $M \equiv U/c = 0.197$, where c is the local speed of sound. This is in the relevant upstream Mach number range described by Anthoine.[1] The upstream Mach number M was set by fixing the the contraction ratio $S_2/S_1 = 1/3$ as described in appendix D, where S_1 and S_2 are the upstream channel height and the throat height, respectively. The vortex was generated at a distance $h = 0.4S_1$, measured from the lower channel wall to center of the vortex.

To record the upstream acoustic response p' a probe is placed at $\mathbf{x}_{\text{probe}} = (-2.75, 0.5)S_1$ at a distance $\Delta x = 7.25S_1$ upstream from the nozzle inlet (Fig. 4). This probe records the pressure $p_{\text{probe}} = p_{\text{probe}}(t)$ at this point. The acoustic response is determined using $p' = p_{\text{probe}}(t) - p_{\text{probe}}(t_{\text{end}})$. The simulations are run for a time sufficiently long so that at the end, when $t = t_{\text{end}}$, the field has returned to its stationary base flow state. The acoustic response due to vortex-nozzle interaction was found to be a plane wave. This was verified using two additional probes placed at $(-2.75, 0.52)S_1$ and $(-2.75, 0.75)S_1$, as indicated with the open circles in Fig. 4.

It is observed that sound is produced by a time-dependent-reaction force acting on the fluid from the nozzle

American Institute of Aeronautics and Astronautics

(a) $t_{\text{emission}}U/S_1 \simeq 4.6$

(b) $t_{\text{emission}}U/S_1 \simeq 5.3$

(c) $t_{\text{emission}}U/S_1 \simeq 6.$

(d) $t_{\text{emission}}U/S_1 \simeq 6.5$

(e) $t_{\text{emission}}U/S_1 \simeq 6.8$ **the acoustic response peak occurs here**

(f) $t_{\text{emission}}U/S_1 \simeq 7.1$
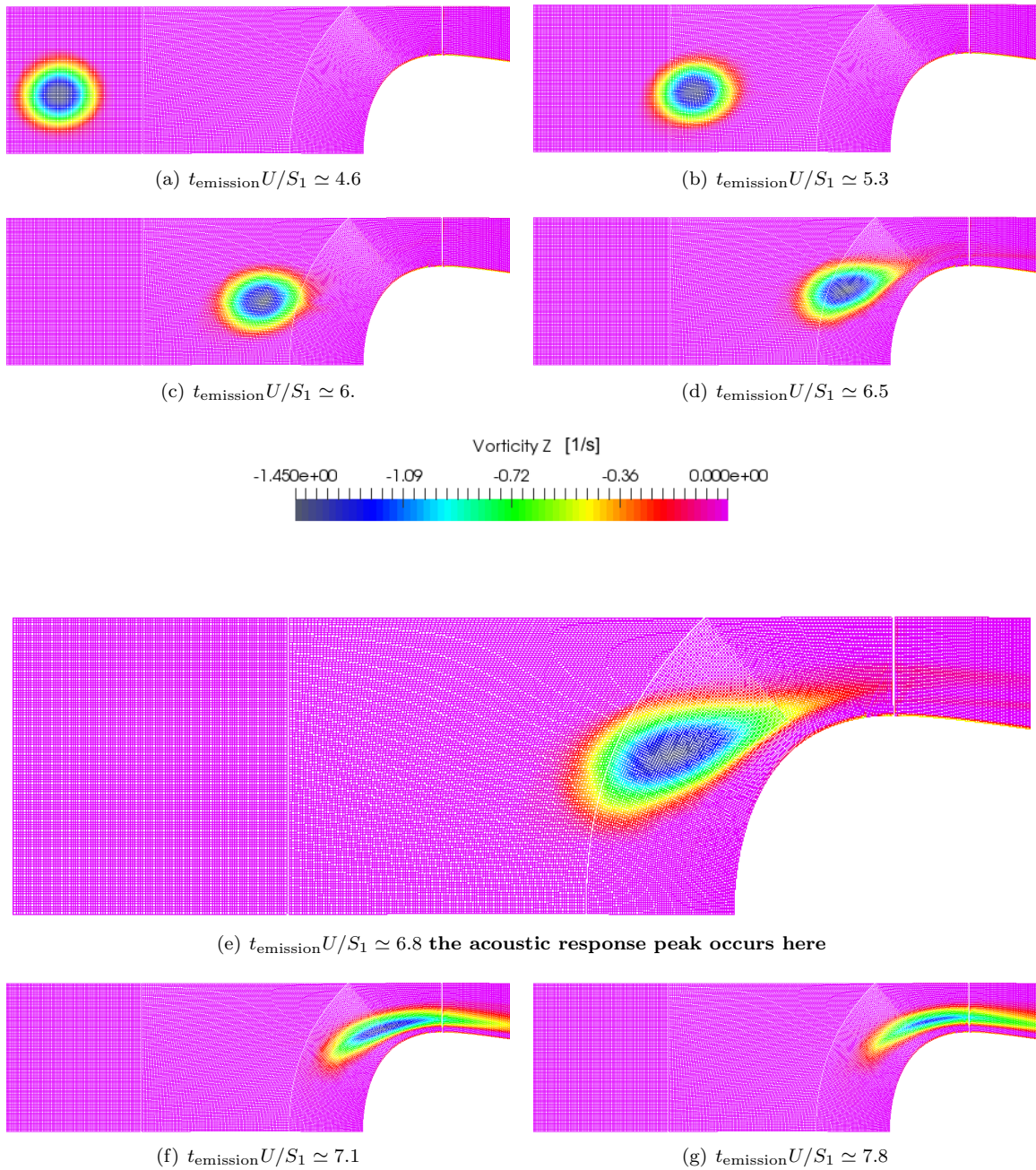
(g) $t_{\text{emission}}U/S_1 \simeq 7.8$

Figure 3. Vortex of dimensionless circulation $\tilde{\Gamma} = -0.86$ and vortex-core radius $R_\Gamma = 0.3S_1$ passing through a right angle inlet nozzle. The vortex is released from $(-2, 0.4)S_1$ i.e. the vortex release height is $h = 0.4S_1$. The dimensionless vortex circulation used here is within the range expected in SRMs.[12] One observes that during the ingestion process no impingement of the vortex and the contraction wall takes place.

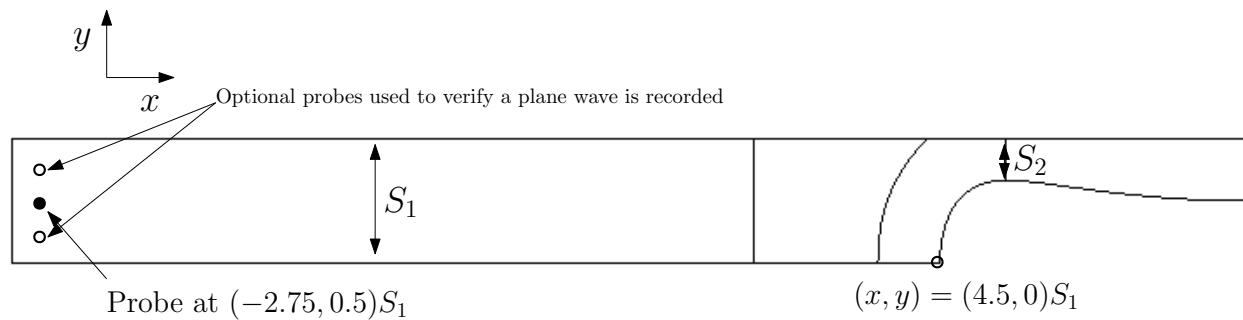American Institute of Aeronautics and Astronautics

Figure 4. Positions of the probe for acoustic response recording, the position of the probe is highlighted with a black dot at $(-2.75, 0.5)S_1$. Two optional probes are placed at $(-2.75, 0.25)S_1$ and $(-2.75, 0.75)S_1$ are indicated with the circles.

wall. The latter is induced by the dynamics of the vortex. Specifically, the moving vortex induces a force on the nozzle wall, which through Newton's third law causes sound production. The sound pulse produced can be related to the position of the vortex using the concept of emission time, t_{emission}, which is the time corrected for time it takes the acoustic wave to reach the probe coming from the nozzle. This is approximated as:

$$t_{\text{emission}} = t - \frac{\Delta x_{\text{probe}}}{c - U}. \tag{1}$$

In Fig. 5 the dimensionless signal $2p'/(\rho U^2)$ recorded by the probe at $\mathbf{x}_{\text{probe}} = (-2.71.05)S_1$ is shown as a function of the dimensionless emission time $t_{\text{emission}}U/S_1$. The labels (a), (b),...to (g), correspond to the stages of vortex-nozzle interaction shown in Fig. 3. One notices that the upstream traveling acoustic pulse produced due vortex-nozzle interaction is generated on approach to the contraction. Note that no impingement is necessary for sound to be produced.
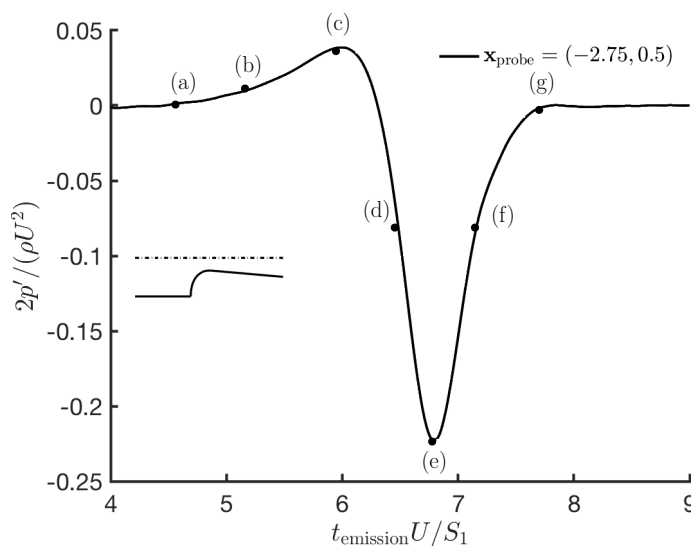

Figure 5. Example of acoustic response signal recorded at probe $(-2.75, 0.5)S_1$. The labels (a), (b)...to (g) correspond to different stages of vortex-nozzle interaction shown on Fig. 3.

American Institute of Aeronautics and Astronautics

IV. Conclusion

In this paper, evidence is reported that for vortex driven indirect sound in SRMs the concept of impingement is not required to account for significant sound production. Indeed, impingement as described in the literature would involve sound production due to vortices physically striking the nozzle walls.[2–7] Instead, dedicated numerical simulations point to sound production due to vortex-nozzle interaction occurring on approach to the contraction (Fig. 3 and Fig. 5), without contact of the vortex with the nozzle walls.

Sound is produced by a fluctuating reaction force of the wall due to the hydrodynamic pressure fluctuation induced by the vortex. There is, as substantiated in this paper, no need for direct contact of the vorticity patch with the wall. Furthermore, the maximum of pressure perturbation is generated during the approach of the vortex to the nozzle, not during the ingestion (passage through the throat). Namely, sound production occurs upstream from the nozzle throat, in a low-Mach-number region.

Acknowledgments

Appendix

A. Euler two-dimensional plane model

In this appendix, a description of the governing equations used for the Euler model are given (appendix B). The meshing process is discussed in appendix C. The establishment of a stationary base flow to initialize vortex-nozzle interaction simulations is described in appendix D. Setting up a vortex-nozzle interaction simulation and the detection of the acoustic response produced is described in appendix E.

B. The governing Euler equations

The governing equations solved by the Euler Internal Aeroacoustics code (EIA) are the following

$$\frac{\partial \rho}{\partial t} + \nabla \cdot [\rho \mathbf{v}] = 0 \tag{2}$$

$$\frac{\partial \rho \mathbf{v}}{\partial t} + \nabla \cdot \{\rho \mathbf{v}\mathbf{v} + p\mathbf{1}\} = \rho \mathbf{f} \tag{3}$$

$$\frac{\partial \mathcal{E}_t}{\partial t} + \nabla \cdot [(\mathcal{E}_t + p)\mathbf{v}] = \mathcal{Q}_E \tag{4}$$

where $\mathcal{E}_t = \rho(e + \mathbf{v}^2/2)$ is the total energy density (total energy per unit volume), $\rho \mathbf{f}$ external momentum source density and $\mathcal{Q}_E$ the energy source. The external momentum source $\mathbf{f}$ is used to generate vortices, a description of this process is provided in appendix E. The energy source term $\mathcal{Q}_E$ is an optional external energy source which can be used to generate entropy spots and can be used for entropy control during vortex generation.[18] The entropy control option was found to have marginal influence on the results. Thus, it was not used for the results described in this text. The ideal gas law is used as an equation of state with a Poisson ratio of 1.4.

C. Mesh generation

In Fig. 6 the mesh for the nozzle configuration with a right angle inlet is shown. The mesh consists of from left to right Blocks 1 (green), 2 (red), 3 (yellow) and 4 (blue). Vortices are generated in Block 1, in this block the cells have a square shape. The vortices are generated by application of a non-uniform external force density $\rho \mathbf{f}$, see appendix E, in this block. Block 2 serves as a transition from the generation block to Block 3. This is done to gradually change the mesh geometry while keeping the cells as square as possible.

Block 3 contains the contraction (nozzle). The lower wall of the contraction in Block 3 is generated using the Henrici transformation[10] as in the analytical model.[15] Block 4 is the diverging channel downstream from the contraction. The height of the upstream channel is S_1 and that of the throat is S_2. The contraction ratio S_2/S_1 of the mesh in Fig. 6 is 3, which corresponds, for a critical nozzle, to an upstream Mach number of $M = 0.197$. This contraction ratio can be varied to change the upstream Mach number M. The discussion is restricted to choked nozzles.

Figure 6. Example of right angle inlet nozzle mesh.

The number of points of the mesh is determined by the need to have a sufficient number of points per vortex-core radius R_Γ, to ensure one is on the convergence domain. To do spatial integration during vortex-nozzle interaction simulations a second order total variation diminishing (TVD) Roe approximate Riemann solver with a van Leer limiter is used.[22] Using three meshes with 36, 54 and 81 points per vortex-core radius $R_\Gamma = 0.3S_1$ the estimated order of accuracy[16] was determined to be 1.8 with a discretization error of approximately 1% for the current mesh.

Thus meshing with 120 points on the upstream inlet wall ensures that 36 points per vortex-core radius $R_\Gamma = 0.3S_1$ is sufficient. Fixing the number of points on the lefthand (inlet) boundary of Block 1 fixes the number of points on the righthand side of Block 1 as well as the left- and righthand sides of Block 2. This is because the number of points on opposing sides of blocks have to be equal. Furthermore, the number of points on the upper and lower channel walls of Block 1 are chosen such that the resulting cells are square. The change of cells surface from cell to cell should be kept as small as possible. In addition, the number of points on the sides of the individual blocks was kept divisible by 4 as a three level explicit multi-grid (EMG) method is used to initialize the Euler model base flow.[17, 18] The initialization procedure of the Euler model base flow is briefly described in appendix D.

D.   Initialization of the Euler model base flow without presence of vortex

Before vortex nozzle interaction can be studied the Euler solution without vortices in the domain has to be initialized i.e. a stationary base flow has to be calculated. This base flow is used as an initial condition for the vortex-nozzle interaction simulations. The boundary conditions[17] imposed to find the base flow are as listed below.

- "Usoft" boundary condition on the upstream wall (on the lefthand side of Fig. 6) this boundary condition imposes:
    - a desired normal time averaged inflow velocity U_{des},
    - the local speed of sound (which is set to one),
    - the local density (which is set to one).

- Wall boundary conditions on the lower and upper walls of the channel associated to a vanishing normal velocity component.

- Connection boundary conditions on all the interfaces connecting the constituent blocks of the channel.

American Institute of Aeronautics and Astronautics

- Non-reflective boundary condition on the downstream end boundary.

Choked nozzles are considered, to determine the upstream inlet velocity U_{des} imposed, the quasi-one dimensional isentropic approximation:

$$\frac{S_2}{S_1} = M \left(\frac{\gamma + 1}{2(1 + \frac{\gamma-1}{2}M^2)} \right)^{\frac{\gamma+1}{2(\gamma-1)}} \tag{5}$$

where γ is the Poisson constant for diatomic gas. The equation is solved numerically to determine which inlet Mach number M corresponds to the critical Mach number for choking. As the local speed of sound is set to one using the "usoft" boundary condition, the value of the calculated upstream inlet Mach can be ascribed directly to U_{des}.

The individual blocks of the mesh are given initial values for the density ρ_{initial}, velocity $\mathbf{v}_{\text{initial}} = (u, v)$ and pressure p_{initial}. For the case of the right angle nozzle inlet (Fig. 6) in Blocks 1, 2 and 3 the following values are set, $\rho_{\text{initial}} = 1$, $\mathbf{v}_{\text{initial}} = (U_{\text{des}}, 0)$ and $p_{\text{initial}} = c^2 \rho_{\text{initial}}/\gamma$ the speed of sound c is fixed to one in the upstream blocks 1 and 2 through the "usoft" boundary condition.[17] In the downstream section of the mesh (Block 4) the values are set to $\rho_{\text{initial}} = 1$, $\mathbf{v}_{\text{initial}} = (1, 0)$ and $p_{\text{initial}} = c^2 \rho_{\text{initial}}/(2\gamma)$. The pressure in Block 4 is lower by a factor two compared to the upstream Blocks 1, 2, and 3. This ensures that no shock wave occurs downstream from the sonic line in the contraction viz. that the flow that will ultimately be reached remains supersonic in Block 4.

The initial condition base flow (IC) to be used for vortex-nozzle interaction simulations is calculated using a three level explicit multi grid relaxation scheme. Spatial integration is performed using a second order total variation diminishing (TVD) Roe approximate Riemann solver with a van Leer limiter.[17, 22] Time marching is done with a (5,2) Runge-Kutta scheme with a Courant number $Co = 3$.[17] The calculation is run for a hundred-thousand (10^5) time steps. A resulting IC for a contraction ratio $S_1/S_2 = 3$ or an upstream inlet Mach number $M = 0.197$ is shown in Fig. 7.

E.   Vortex generation and boundary conditions used for vortex-nozzle interaction

To study vortex-nozzle interaction a vortex needs to be generated. This is done in a vortex-less base flow, the establishment of which is described in appendix D. The stationary base flow is used to initialize the domain in which vortex-nozzle interaction simulations are carried out.

The boundary conditions used in vortex-nozzle interaction simulations are as follows.

- An acoustically non-reflective condition is used on the upstream wall on the lefthand side in Fig. 6. This boundary condition mimics a connection to an infinite upstream channel and it maintains the local average inflow velocity, density and sound speed imposed by the base flow as an initial condition.

- Wall boundary conditions on the lower and upper walls of the channel.

- Connection boundary conditions on all the interfaces connecting the constituent blocks of the channel.

- Non-reflective boundary condition on the downstream end boundary.
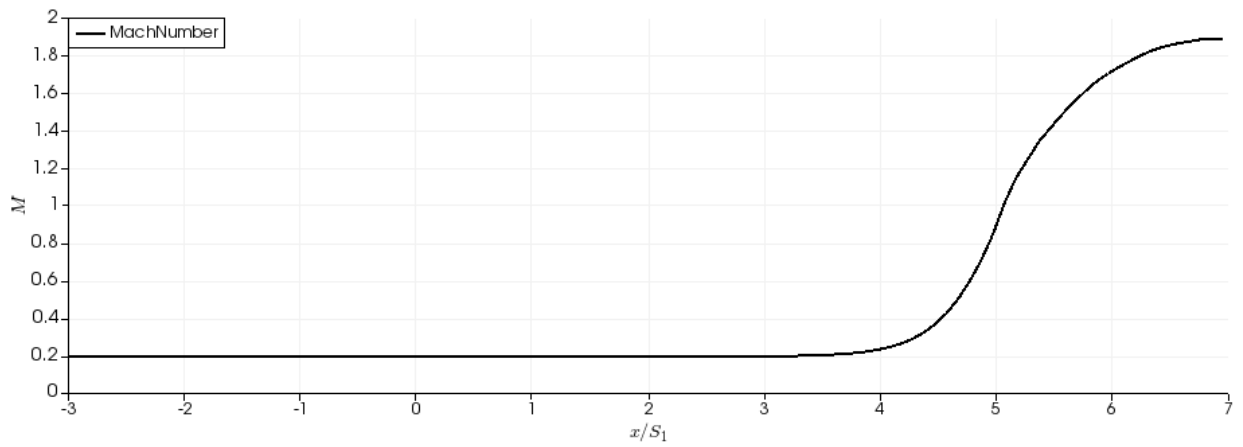
A few snapshots of a vortex during the generation process are shown in Fig. 8. These snapshots are obtained with an upstream Mach number $M = 0.197$, release height $h = 0.4S_1$, vortex-core radius $R_\Gamma = 0.3S_1$. The point at which the generation process of this vortex is started is $\mathbf{x}_0 = (x_0, y_0) = (-2, 0.4)S_1$.

To generate a fully mature vortex like the one shown in Fig. 8 (c) a momentum source $\mathbf{f}$ is used. This source causes the generation of a vortex by means of local injection of momentum around a point, which is advected with the base flow[a]. The momentum source $\mathbf{f} = (f_x, f_y)$ used is

---

[a]At low Mach numbers $M^2 < 1$ the two dimensional vorticity transport equation is $\frac{\partial \omega_z}{\partial t} + \mathbf{v} \cdot \nabla \omega_z = \frac{\partial f_y}{\partial x} + \frac{\partial f_x}{\partial y}$ i.e. to generate a vortex the momentum source $\mathbf{f}$ has to be convected with the flow.[21]

American Institute of Aeronautics and Astronautics
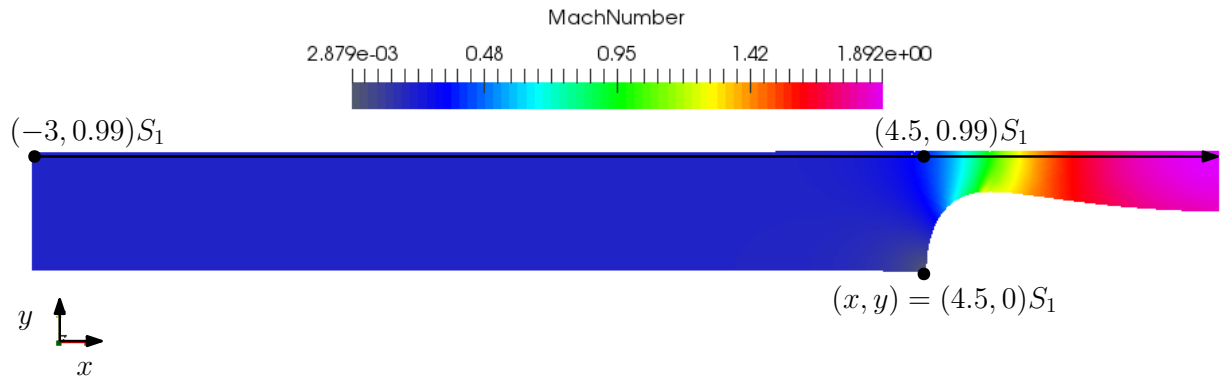
(a) Initial condition base flow for critical nozzle contraction ratio $S_1/S_2 = 3$ i.e. an upstream inlet Mach number $M = 0.197$

(b) Value of the local Mach number along the arrow at $y = 0.99$ viz. close to the symmetry line in the $x-y$ plane shown in (a).

Figure 7.   Initial condition base flow for $M = 0.05$.

Vorticity Z [1/s]

-1.450e+00   -1.09   -0.72   -0.36   0.000e+00

(a) $tU/S_1 \simeq 0.59$

(b) $tU/S_1 \simeq 2.1$
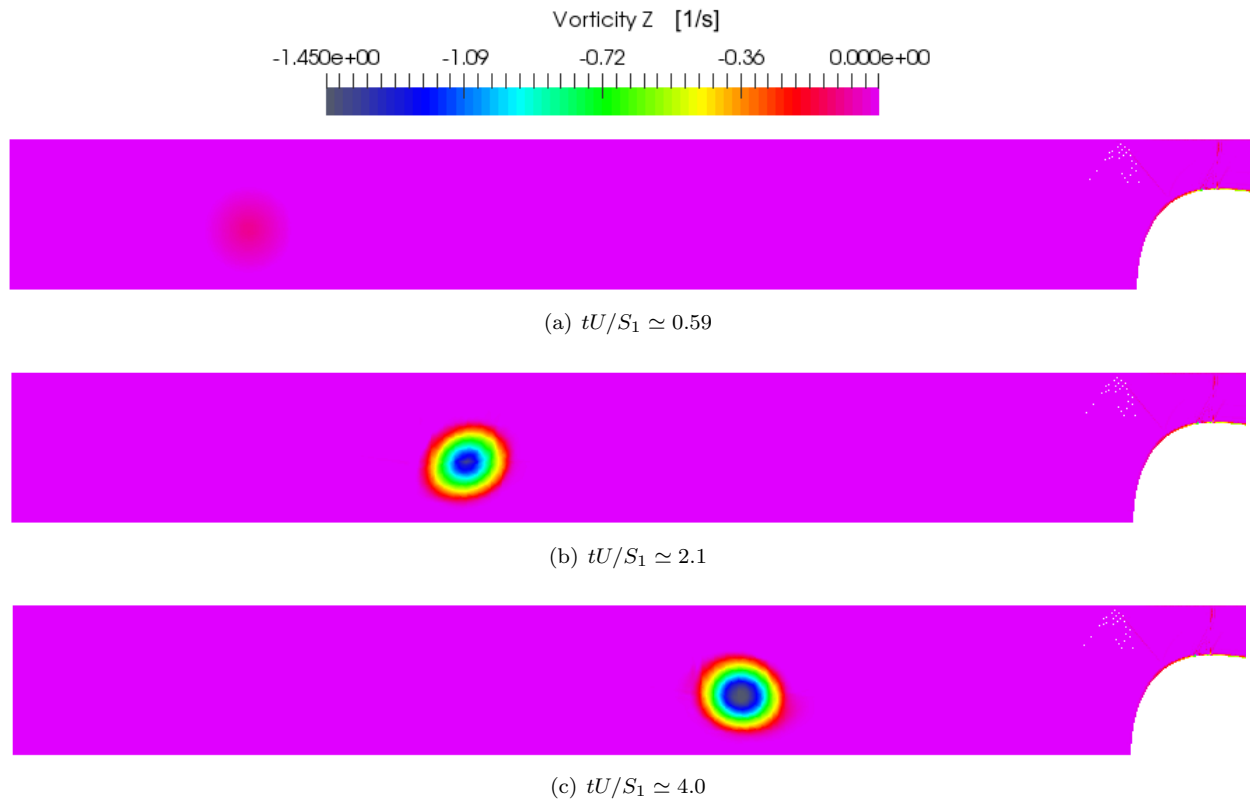
(c) $tU/S_1 \simeq 4.0$

Figure 8. Snapshots of vortex during the generation process. The results shown here are obtained with upstream Mach number $M = 0.197$, release height $h = 0.4S_1$, vortex-core radius $R_\Gamma = 0.3S_1$. The generation time interval is $0 \leq t/U/S_1 \leq 3.0$. In subfigures (a) and (b) the vortex is still being generated, whilst in subfigure (c) a fully mature vortex with vortex circulation $\tilde{\Gamma} = -0.86$ is shown.

American Institute of Aeronautics and Astronautics

$$f_x = \mathcal{A}_{\text{local}} \sin(\theta) \tag{6}$$

$$f_y = -\mathcal{A}_{\text{local}} \cos(\theta) \tag{7}$$

where the angle θ is defined in Fig. 9. The position of a point $\mathbf{x}_{\text{relative}}$ with respect to the moving source center is described in polar coordinates $\mathbf{x}_{\text{relative}} = r(\cos(\theta), \sin(\theta))$ with $r = |\mathbf{x}_{\text{relative}}|$. The amount of momentum injected varies with respect to the distance r from the source center which moves with the flow, where by definition $r > 0$. This variation is controlled by a local $\mathcal{A}_{\text{local}}$ amplitude which depends on the distance r as follows
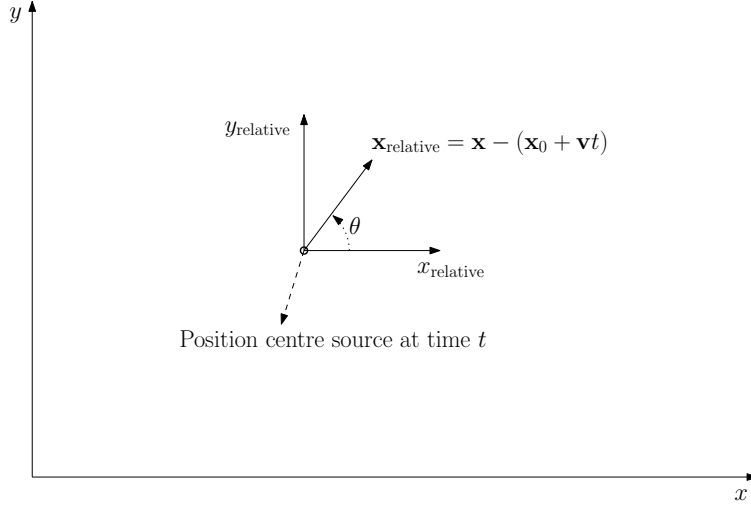

Figure 9. Definition of relative coordinates for the momentum source f. The position of a point with respect to the moving source center is described with local polar coordinates viz. $\mathbf{x}_{\text{relative}} = r(\cos(\theta), \sin(\theta))$ with $r = |\mathbf{x}_{\text{relative}}|$.

$$\mathcal{A}_{\text{local}} = \frac{\mathcal{A}_{\text{core}}}{2\pi r} \tag{8}$$

were the core amplitude $\mathcal{A}_{\text{core}}$ is

$$\mathcal{A}_{\text{core}} = \begin{cases} \mathcal{A} \left[-2\left(\frac{r}{R_\Gamma}\right)^3 + 3\left(\frac{r}{R_\Gamma}\right)^2 \right] & \text{if } 0 \leq \frac{r}{R_\Gamma} \leq 1 \\ \mathcal{A} \text{ if } \frac{r}{R_\Gamma} \geq 1 \end{cases} . \tag{9}$$

One observes that the local momentum source is irrotational ($\nabla \times \mathbf{f} = 0$) for $r > R_\Gamma$ and falls of as a hyperbola, the net effect is that vorticity is only produced for $r < R_\Gamma$. The vortex-core radius R_Γ is a user chosen quantity. The local amplitude $\mathcal{A}_{\text{local}}$ depends on a global amplitude $\mathcal{A}$. This global amplitude is determined as follows

$$\mathcal{A} = \begin{cases} 0.5\mathcal{A}_{\text{max}} \left[1 - \cos\left(\frac{\pi t}{\tau_{\text{start}}}\right) \right] & \text{if } 0 \leq t \leq \tau_{\text{start}} \\ \mathcal{A}_{\text{max}} \text{ if } \tau_{\text{start}} \leq t \leq \tau_{\text{start}} + \tau_{\text{max}} \\ 0.5\mathcal{A}_{\text{max}} \left[1 + \cos\left(\frac{\pi(t - (\tau_{\text{start}} + \tau_{\text{max}}))}{\tau_{\text{end}}}\right) \right] & \text{if } \tau_{\text{start}} + \tau_{\text{max}} \leq t \leq \tau_{\text{start}} + \tau_{\text{max}} + \tau_{\text{end}} \\ 0 \text{ for } t > \tau_{\text{start}} + \tau_{\text{max}} + \tau_{\text{end}} \end{cases} \tag{10}$$

where the maximum global amplitude $\mathcal{A}_{\text{max}}$, the startup time τ_{start} of generation, the amount of time τ_{max} at which the generation is done with the maximum global amplitude, the time τ_{end} during which the generation process is ramped down are chosen by the user and $t = t_{\text{end}}$ is the time at which the simulation ends. In this scenario, the vortex generation comprises three phases of duration τ_{start}, τ_{max} and τ_{end}.

American Institute of Aeronautics and Astronautics

In Fig. 10 an example of the evolution of the dimensionless vortex circulation from $\tilde{\Gamma} = 0$ to -0.86 during the generation process is shown. The results shown in Fig. 10 are obtained with maximum amplitude $\mathcal{A}_{max} = 1.92 \times 10^{-2}$, $R_\Gamma/S_1 = 0.3$, $\tau_{start}U/S_1 = 1.18$, $\tau_{max}U/S_1 = 0.592$ and , $\tau_{end}U/S_1 = 1.18$. The initial position of the vortex was $\mathbf{x}_0 = (-2, 0.4)S_1$ corresponding to an upstream vortex release height $h = 0.4S_1$. In Fig. 11 the vorticity distribution for this case is shown at four different times: during the startup phase, during the generation with $\mathcal{A}_{max}$, the end of vortex generation and full maturity. When the generation process is completed the vortex circulation is conserved.
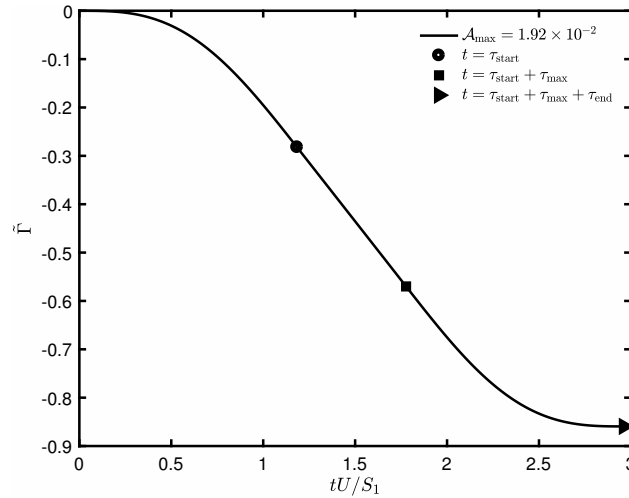

Figure 10. Generation phase of vortex circulation $\tilde{\Gamma} = -0.86$. To generate this vortex the user choses the amount time during which of the vortex is being generated with the maximum global amplitude $\mathcal{A}_{max}$ which in this case is $\tau_{max}U/S_1 = 0.592$ and $\mathcal{A}_{max} = 1.92 \times 10^{-2}$ respectively. The amount of time it takes to ramp up the global vortex generation amplitude $\mathcal{A}$ to this user set maximum is user difined and in this case equal to $\tau_{start}U/S_1 = 1.18$. To ramp it down the generation process the global amplitude $\mathcal{A}$ is lowered to zero in a time interval $\tau_{end}U/S_1$, which in this case is 1.18. The end of intervals τ_{start}, τ_{max} and τ_{end} are indicated with a circle, a square and side-ways triangle respectively.

References

[1] J. Anthoine. *Experimental and numerical study of aeroacoustic phenomena in large solid propellant boosters, with application to the Ariane 5 solid rocket motor*. PhD thesis, Université Libre de Bruxelles, Belgium, 2000.

[2] F. E. C. Culick. *Unsteady Motions in Combustion Chambers for Propulsion Systems*, volume RTO-AG-AVT-039 of *RTO AGARDograph*. RTO/NATO, 2006.

[3] K.W. Dotson, S. Koshigoe, and K.K. Pace. Vortex shedding in a large solid rocket motor without inhibitors at the segmented interfaces. *Journal of Propulsion and Power*, 13(2):197–206, 1997.

[4] Y. Fabignon, J. Dupays, G. Avalon, F. Vuillot, N. Lupoglazoff, G. Casalis, and M. Prévost. Instabilities and pressure oscillations in solid rocket motors. *Aerospace Science and Technology*, 7(3):191–200, 2003.

[5] V. Ferretti. *Numerical Simulations of Acoustic Resonance of Solid Rocket Motor*. PhD thesis, La Sapienza, University of Rome, 2011.

[6] V. Ferretti, B. Favini, E. Cavallini, F. Serraglia, and M. Di Giacinto. Vortex-sound generated pressure oscillations simulation in internal flow by means of q-1d model. In *4th European conference for aerospace sciences*, 2011.

[7] G. A. Flandro. Vortex driving mechanism in oscillatory rocket flows. *Journal of Propulsion and Power*, 2(3):206–214, 1986.

[8] S. Gallier and F. Godfroy. Aluminum Combustion Driven Instabilities in Solid Rocket Motors. *Journal of Propulsion and Power*, 25(2):509–521, 2009.

[9] S. Gallier, M. Prevost, and J. Hijlkema. Effects of cavity on thurst oscillations in subscale solid rocket motors. In *45th AIAA/ASME/ASEE Joint Propulsion Conference & Exhibit*, number 2009-5253. AIAA, 2009.

[10] P. Henrici. *Applied and Computational Complex Analysis*, volume I. Wiley-Interscience, NY, USA, 1974.

[11] L. Hirschberg. *Low order modeling of vortex driven self-sustained pressure pulsations in solid rocket motors*. PhD thesis, CentraleSupélec, Université Paris Saclay, 2019.

[12] L. Hirschberg, S. J. Hulshoff, J. Collinet, C. Schram, and T. Schuller. Vortex nozzle interaction in solid rocket motors: A scaling law for upstream acoustic response. *The Journal of the Acoustical Society of America*, 144(1):EL46–EL51, 2018.

[13] L. Hirschberg, T. Schuller, J. Collinet, C. Schram, and A. Hirschberg. Analytical model for the prediction of pulsations in a cold-gas scale-model of a solid rocket motor. *Journal of Sound and Vibration*, 419:452–468, 2018.
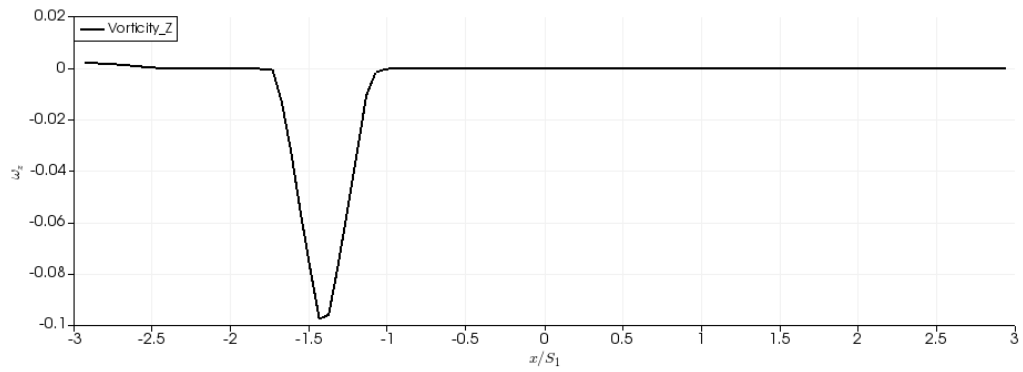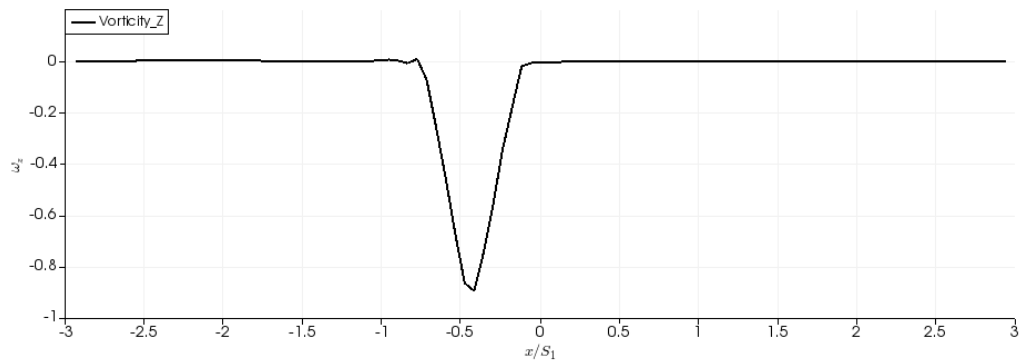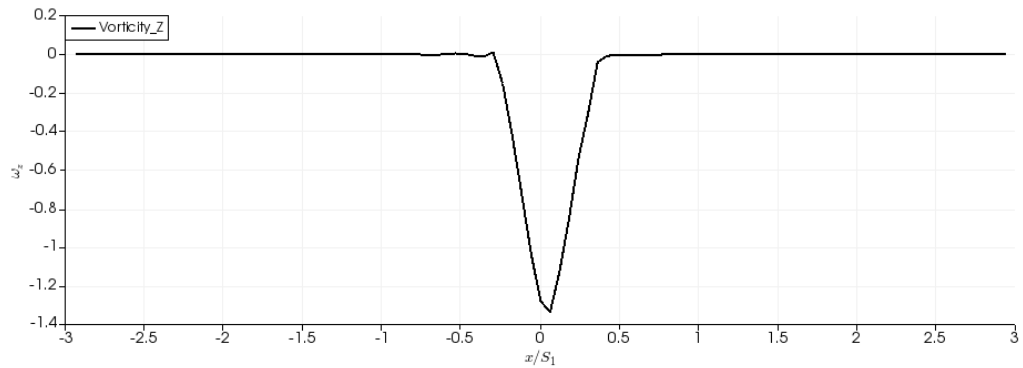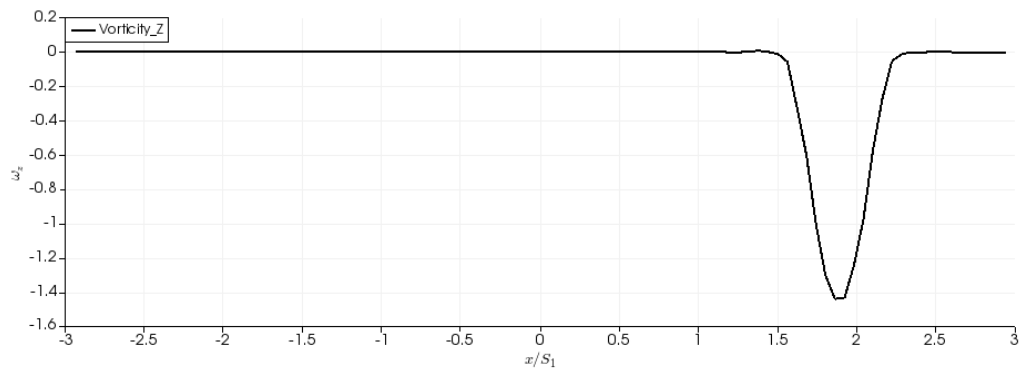
(a) $tU/S_1 \simeq 0.59$ during the startup phase

(b) $tU/S_1 \simeq 1.6$ during the maximum generation phase

(c) $tU/S_1 \simeq 2.1$ during the end phase

(d) $tU/S_1 \simeq 4.0$ at full maturity after the completion of the vortex generation phases

Figure 11. The vorticity ω_z distribution along a line at $y = 0.4S_1$ at different stages of vortex generation for a vortex of $\tilde{\Gamma} = -0.86$.

American Institute of Aeronautics and Astronautics

[14]L. Hirschberg, T. Schuller, C. Schram, and J. Collinet. Lumped model for vortex sound in large solid rocket motors. In *24th AIAA/CEAS Aeroacoustics conference*. AIAA, June 2018.

[15]L. Hirschberg, T. Schuller, C. Schram, J. Collinet, M. Yiao, and A. Hirschberg. Interaction of a vortex with a contraction in a 2-dimensional channel: incompressible flow prediction of sound pulse. In *23rd AIAA/CEAS Aeroacoustics conference*, 2017.

[16]S. J. Hulshoff. *Computational modelling: lecture notes*. TU Delft, 2016.

[17]S. J. Hulshoff. *EIA an Euler Code for Internal Aeroacoustics: method description and user's guide*. Faculty of Aerospace Engineering, Delft University of Technology, Delft, the Netherlands, October 2016.

[18]S. J. Hulshoff. Private communication. During a visit at TU Delft, February 15th 2018.

[19]S. J. Hulshoff, A. Hirschberg, and G. C. J. Hofmans. Sound production of vortex nozzle interaction. *Journal of Fluid Mechanics*, 439:335–352, 2001.

[20]D. Rockwell. Oscillations of impinging shear layers. *AIAA Journal*, 21(5):645–664, 1983.

[21]P. G. Saffman. *Vortex Dynamics*. Cambridge University Press, UK, 1992.

[22]V. Venkatakrishnan and A. Jameson. Computation of unsteady transonic flows by the solution of euler equations. *AIAA Journal*, 26(8):974–981, 1988.